Numerical investigation of the coexistence of multiple tones in flow-induced cavity noise*

Xavier Gloerfelt†, Christophe Bogey‡, and Christophe Bailly§

Laboratoire de Mécanique des Fluides et d'Acoustique
Ecole Centrale de Lyon & UMR CNRS 5509
69134 Ecully, France.

Abstract

Flow-induced cavity oscillations are often characterized by the presence of multiple simultaneous peaks in the spectra. This phenomenon is investigated numerically by using Direct Noise Computations for Mach 0.6 flows over cavities with a length-to-depth ratio of $L/D = 1$. Two parameters are studied : the width of the cavity in the spanwise direction, and the thickness of the incoming boundary layer. The dominant oscillation frequencies correspond to the number of vortices in the shear layer. Low-frequency components and higher harmonics are also identifiable in the spectra. Time-frequency analyses show that the multiple tones do coexist. Even if some low frequencies can be associated to lower Rossiter modes, the coexistence is not attributable to switching between competitive modes. In general, the low-frequency components do not result directly from vortex coalescence, although such interaction are not precluded. They arise instead from severe modulations in the vortex-corner interactions, leading to remarkably ordered cycling patterns. To understand to what extent quadratic nonlinearities are important, bispectral analysis has been performed. All the components observed in the spectra may be related to the sum and difference of the primary cavity modes, and eventual harmonics, through nonlinear interactions. This mutual interaction involving nonlinear triads is a candidate explanation for the coexistence of multiple self-sustained cavity tones.

1. Introduction

The noise radiated by a flow past a cavity has been widely studied during the last fifty years because of its practical interest and because of the variety of theoretical questions that it raises. A complex feedback process sustains coherent oscillations in the shear layer developing above the cavity, leading to important radiated noise. This noise consists of intense discrete and broadband components. The present study focuses on the multiple discrete tones that often characterize cavity flow spectra.

The coexistence of tones is a very complicated problem, insofar as the peaks can have different physical origins. The turbulent shear layer spanning the cavity open acts as a broadband noise source which can drive longitudinal or depth resonance modes of the cavity box closed by the shear layer or the Helmholtz resonance depending on the cavity opening and volume. It was postulated as the basic phenomenon by Plumblee *et al.*[1] in 1962. This source of excitation of cavity resonance was noticed experimentally by Elder *et al.*[2] who called it *turbulent rumble*. However this phenomenon was not sufficient to explain the even louder pressure peaks noted in experiments with laminar flows over nonresonant cavities. A sequence of non-harmonic tones is usually observed. Rossiter[3] in 1964 is one of the first investigator who related the flow oscillations to the presence of concentrated vortices. The self-sustained selection results from an aeroacoustic feedback loop, as described by Powell[4] (1961) in the case of the jet-edge interaction. Kelvin-Helmholtz-type instabilities shed periodically in the shear layer near the upstream separation corner grow during convection toward the downstream edge. A sound pulse is generated when these vortical structures reaches the downstream edge, then propagates upstream and excites the shear layer formation. A vortex travels across the cavity in time L/U_c, where U_c is the convection velocity of the vortical structures, whereas the sound radiates back to the upstream edge in time L/c_0, c_0 denoting the speed of sound. The feedback pressure wave must attain the upstream edge just at the right instant to reinforce the periodic shedding, so that the frequency f satisfies Rossiter's equation :

$$\frac{L}{U_c} + \frac{L}{c_0} = \frac{n}{f}$$

where n is an integer representing the number of vortices in the shear layer. To agree with measurements, Rossiter replaced n by $n - \alpha$, where α was interpreted as

†Post-doc

‡Research scientist CNRS

§Assistant Professor, Member AIAA

a constant phase lag corresponding to a time delay between the vortex arrival at the impingement corner and the emission of the acoustic pulse. Blake[5] included also in this constant the eventual time delay between the arrival of the sound at the upstream edge and the release of new instabilities in the shear layer. Rossiter's formula is usually expressed as :

$$\mathrm{St} = \frac{fL}{U_\infty} = \frac{n-\alpha}{\frac{U_\infty}{U_c} + \mathrm{M}} \qquad n = 1, 2, ...$$

where M is the ratio between the freestream flow velocity U_∞ and the sound speed c_∞. At high subsonic to supersonic Mach numbers, this simple equation succeeds in predicting the admissible Strouhal numbers, although it provides no information on the amplitude of the self-sustained oscillations nor it indicates which of the multiple peaks will be predominant. At low Mach numbers, the acoustic response of the cavity can superimpose on the aeroacoustic feedback. For frequencies close to that of the acoustic resonances, the acoustic forcing by the cavity resonance can overwhelm that provided by the impingement pulse. As clearly demonstrated in the experiments of Elder[2] or Meissner[6] varying the cavity parameters, the multiple peaks can correspond to acoustic resonances excited successively by the *turbulent rumble*, then by the Rossiter feedback loop. The resonant frequency (*pipe tone*) can coexist with several Rossiter's modes (*cavity tones*). A double resonance is observed when two peaks are coincident.

In the present work, numerical simulations are performed to shed light on this complex process. Low Reynolds number configurations are chosen to avoid contribution from the rumble excitation to the multiple frequency content. This also allows to achieve well-resolved 3-D Large Eddy Simulations (LES) at a reasonable computational cost. Long-time simulations are then possible to perform fine spectral analysis. A subsonic Mach number M=0.6 is chosen to ensure that the mechanism driving the oscillations is the Rossiter feedback loop. The shape ratio is taken as $L/D = 1$, which is the limit between the shallow and the deep cavities. For these intermediate ratios, the question of the selection of a dominant mode remains whole. Tam & Block[7] or Ahuja & Mendoza[8] observed a complex alternance between the admissible modes.

Two parameters are examined in this study, namely the spanwise width of the cavity, and the thickness of the incoming boundary layer. The effects of the first parameter were investigated by Rossiter,[3] and further by Ahuja & Mendoza,[8] who found that the spanwise width weakly affects the periodic frequencies but can have a large influence on the magnitude of the different components. The second parameter, often unknown in the early measurements, was recognized as a determinant factor for the mode selection with the emergence of the shear layer stability theory.[7] As shown by Gharib & Roshko,[9] the ratio of the cavity length over the momentum thickness of the separating boundary layer L/δ_θ participates to the mode selection.

The paper is organized as follows. Section 2 describes the computational modelling. The aerodynamic and acoustic fields obtained from LES are analysed in section 3. The first task is the identification of the various peaks and their relative strength in the autospectra. Time-frequency analysis is used to ascertain whether the different modes coexist or are the result of a mode-switching phenomenon. An additional consideration is to determine to what extent the different components are excited independently or are nonlinearly coupled. Quadratic phase coupling is investigated thanks to bispectral analysis in section 4, and possible mechanisms leading to the coexistence of multiple tones are discussed.

2. Definition of the simulations

2.1 Numerical method

A schematic view of the flow domain is shown in figure 1. The origin of the coordinate system is located at the middle of the upstream corner. For the Direct Noise Computation (DNC), the full three-dimensional compressible Navier-Stokes equations are solved to simulate both the aerodynamic and the acoustic fields.

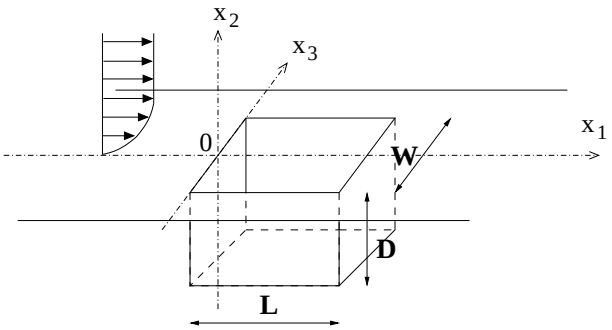

Figure 1: Sketch of the flow domain and coordinate system.

The governing equations are integrated in time using an explicit low-storage six-step Runge-Kutta scheme, optimized in the wave number space. The derivatives are calculated on a slowly nonuniform Cartesian grid by using optimized finite differences with an eleven-point stencil for the convective fluxes, and 4^{th} order finite differences for the viscous and heat fluxes. As part of the algorithm, a selective filtering built on an eleven-point stencil is incorporated in each direction to eliminate grid-to-grid oscillations. The coefficients of the Runge-Kutta, of the finite differences and of the filtering are given in Bogey and Bailly.[10]

The other key point of DNC is the use of non-reflecting conditions for the free-field boundaries of the domain. A three-dimensional formulation of the far-field radiation boundary conditions of Tam and Dong[11] is implemented. It is combined with a sponge zone at the

outflow and lateral boundaries in order to dissipate the vortical structures. This sponge zone uses grid stretching and a progressively applied Laplacian filter. On all solid boundaries, the no-slip conditions are imposed together with the nullity of the normal gradient of pressure.

2.2 Simulation parameters

Four configurations are investigated. The length-to-depth ratio is $L/D = 1$, with $D = 2$ mm, and the freestream Mach number is fixed at M= 0.6, giving a Reynolds number $\mathrm{Re}_D = 28\,700$. The computations are initiated by extrapolating a third-order polynomial expression of the Blasius boundary layer profile into the domain. The freestream air temperature is $T_\infty = 320.26$ K, and the static pressure p_∞ is taken as 1 atm.

Run	Aspect ratio		L/δ_{θ_R}	$\mathrm{Re}_{\delta_{\theta_R}}$
	L/D	L/W		
3Dr1N1	1	1.28	105	272
3Dr1W1	1	0.5	105	272
3Dr1N2	1	1.28	76	377
3Dr1W2	1	0.5	76	377

Table 1: Parameters of the 4 simulations presented. The thicknesses (suffix R) are evaluated at the upstream edge of the cavity when the mean flow is converged.

The characteristics of each configurations are given in table 1. A thin boundary layer is imposed ahead of the cavity in the cases 3Dr1N1 and 3Dr1W1, whereas a thicker one is used in 3Dr1N2 and 3Dr1W2. The spanwise dimension is narrow in 3Dr1N1 and 3Dr1N2, and wide in 3Dr1W1 and 3Dr1W2. The cases 3Dr1N1 and 3Dr1W1 (referred to as 3Dr1N and 3Dr1W) have already been documented in a previous paper.[12] However the transient was not ended in the simulation 3Dr1N.

The nonuniform Cartesian meshes use respectively $41 \times 33 \times 41$ points inside the cavity and $121 \times 132 \times 71$ outside for the narrower cases (N), and $41 \times 33 \times 81$ in the cavity and $121 \times 132 \times 109$ outside for the wider ones (W), clustered near the solid walls. The minimum gridsize corresponds to $\Delta x_2^+ \simeq 4$, giving a time step $\Delta t = 2.8 \times 10^{-8}$ s. Eighty thousand iterations are performed, representing a large amount of cycles, necessary for the bispectral analysis. The computations last 20 and 35 hours on a Nec SX-5 for the narrower and wider configurations respectively.

3. Analysis of the self-sustained oscillations

3.1 Spectral analysis of the pressure signals

Let us first look at the pressure fields for the four configurations. Remind that the parameters investigated, *i.e.* the spanwise cavity dimension and the thickness of the incoming boundary layer, are not taken into account in the Rossiter-like analyses, which thus predict the same

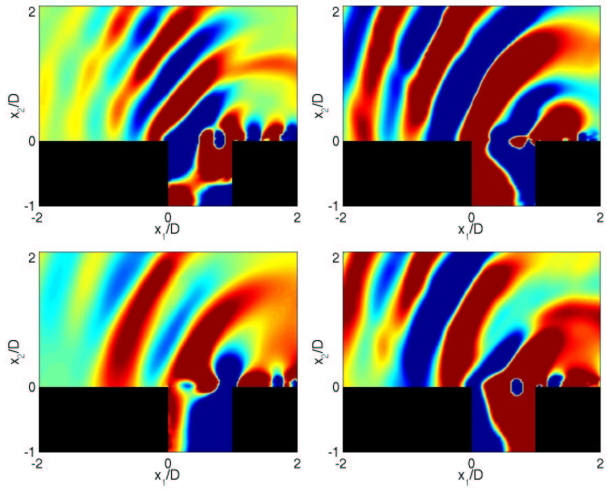

Figure 2: Pressure fields in the midplane $x_3 = 0$ for the 4 simulations : 3Dr1N1 (top left), 3Dr1W1 (top right), 3Dr1N2 (bottom left), and 3Dr1W2 (bottom right). Levels between -500 and 500 Pa.

dominant frequency in all cases. On the contrary figure 2 shows that the influence of these parameters is far from negligible. The principal frequency of acoustic waves is higher for 3Dr1N1. All the radiated fields are marked by a pronounced upstream directivity, resulting from the combination of the convection effects by the flow at M=0.6, and of the interference patterns between the waves directly emitted from the downstream corner region and the waves reflected by the cavity walls. However the main direction of radiation is affected by the preferred sound frequency, and is found to be closer to the upstream axis for lower frequencies. Since the freestream velocity is the same in all cases, this dependence can be explained by changes in the interference patterns between direct and reflected waves. In the low-frequency limit, the wavelength is large relative to the cavity dimensions, so that the radiation is compact, and the direct and reflected waves are almost undistinguishable. At the high frequency of the configuration 3Dr1N1, the lack of compactness results in destructive interference, so that the main direction of the sound radiation is around 50^o from the upstream axis. Another finding is the important difference between the amplitude of the radiated fields of figure 2. The overall sound pressure levels at the point $(-1.16D,3D,0)$ are 146 dB for 3Dr1N1, 152 dB for 3Dr1W1, 140 dB for 3Dr1N2, and 151 dB for 3Dr1W2. The sound levels are greater for the wider cavities.

The spectral content of the pressure field is now analysed. A large amount of averaging is required to converge the Power Spectral Densities (PSD). A high visualisation must also be kept to avoid the smearing of close peaks. Two thousand temporal samples are recorded with a sampling rate $\Delta f = 1/(20\Delta t_{DNC})$. The autoregressive method of Burg is used to enhance the resolution

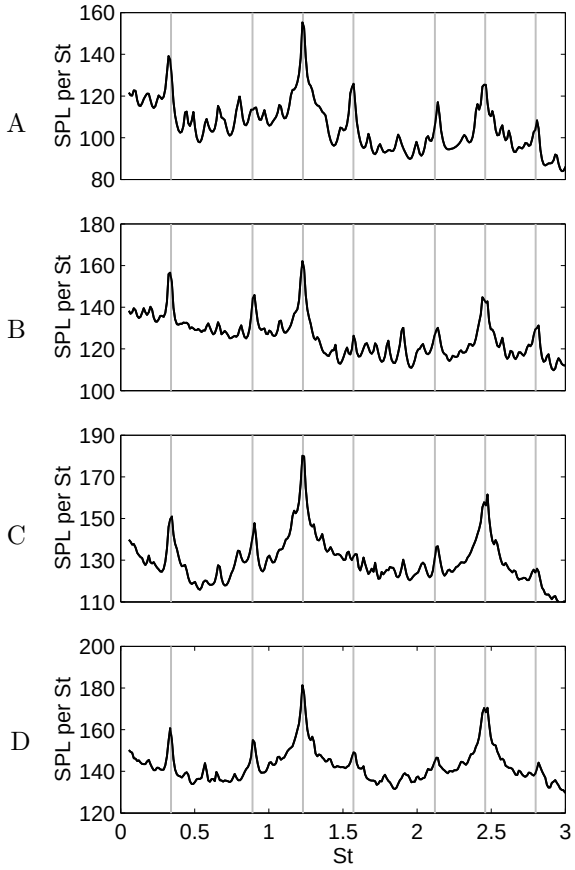

Figure 3: Power spectral density of fluctuating pressure for 3Dr1N1. From top to bottom, spectra at four sensors : A located at (x_1,x_2,x_3)= ($-1.16D$,$3D$,0), B at (0,0.02D,0), C at (D,0.02D,0), and D at ($D/2$,$-D$,0).

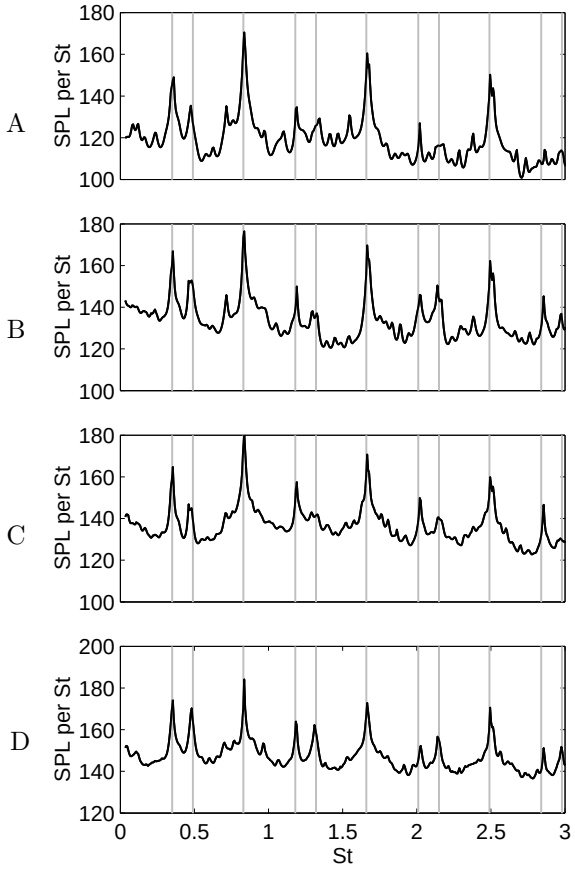

Figure 4: Power spectral density of fluctuating pressure for 3Dr1W1. Same sensors A to D as in fig. 3.

of the peaks (see Marple[13]). The spectra, evaluated at four sensors located respectively in the main acoustic radiation (sensor A), at the beginning (B) and at the end (C) of the shear layer, and at the bottom of the cavity (D), are depicted in figures 3 to 6 for the four simulations. All the spectra are characterized by the presence of multiple well-defined peaks.

Thin incoming boundary layer - 3Dr1N1 & 3Dr1W1

The values of the Strouhal numbers associated to the first peaks are reported in table 2. For the simulation 3Dr1N1, in figure 3, whatever the locations of the sensors may be, 7 peaks are detected for a St$<$ 3. The principal ones are for St_3 and its first harmonic St_6. Another significant peak is observed at St_1, and secondary peaks are visible, equally spaced on both sides of St_3 and St_6. Another characteristic feature is the variations of the relative amplitude of the peaks from one sensor to the other. The low-frequency component St_1 is for example weak at the sensor C near the end of the shear layer, whereas its strength was comparable to that of the dominant tone St_3 at the sensor B near the upstream edge.

Eleven peaks are numbered for St$<$ 3 for the wider cavity 3Dr1W1. Figure 4 indicates that St_3, St_6, and St_9 are the principal tones, corresponding to the fundamental frequency of the acoustic waves, and the first two harmonics. The principal secondary value is St_1. The additional peaks are more marked than in the previous case, especially at the sensors located in the flow or at the cavity floor. They consists in two regularly spaced peaks between the dominant peaks.

Trying to elucidate the strikingly series of the peak values in these first two cases, the following conjecture is made. If the low frequency is denoted f_a, and the dominant frequency f_b, the successive peak frequencies can be expressed as : f_a, $f_b - f_a$, f_b, $f_b + f_a$, $2f_b - f_a$, $2f_b$, $2f_b + f_a$, $3f_b - f_a$, $3f_b$, $3f_b + f_a$, $4f_b - f_a$, $4f_b$, ... In both cases $f_a = f_1$, and $f_b = f_3$. The f_1 values are close ($St_1 \sim 0.34$), whereas the dominant tone is not the same ($St_3 = 1.23$ for 3Dr1N1 and $St_3 = 0.83$ for 3Dr1W1). The above conjecture is verified since the gray lines obtained by using St_1 and St_3 values in the relationships superimpose on the spectral peaks in figures 3 and 4.

Thick incoming boundary layer - 3Dr1N2 & 3Dr1W2

	St_1	St_2	St_3	St_4	St_5
3Dr1N1	0.34	0.89	1.23	1.57	2.12
	($\circ$)	($\square$)	($\triangle$)	($*$)	($\diamond$)
3Dr1W1	0.35	0.48	0.83	1.28	1.31
	($\circ$)	($\square$)	($\triangle$)		

St_6	St_7	St_8	St_9	St_{10}	St_{11}
2.46	2.80				
($\triangle$)					
1.66	2.01	2.24	2.49	2.83	2.98
($\triangle$)			($\triangledown$)		

Table 2: Strouhal numbers corresponding to the spectral peaks for thin boundary layers.

	St_1	St_2	St_3	St_4	St_5
3Dr1N2	0.16	0.32	0.48	0.64	0.80
	($+$)	($\circ$)	($\square$)	($\circ$)	($\triangle$)
3Dr1W2	0.15	0.19	0.33	0.49	0.64
			($\circ$)	($\square$)	($\circ$)

St_6	St_7	St_8	St_9	St_{10}	St_{11}
0.96	1.12	1.28	1.44	1.60	1.76
	($*$)	($\diamond$)			
0.68	0.82	0.97	1.01	1.15	1.31
	($\triangle$)			($*$)	($\diamond$)

St_{12}	St_{13}	St_{14}	St_{15}	St_{16}	St_{17}
1.92	2.80				
1.46	1.50	1.64	1.79	1.83	1.97

Table 3: Strouhal numbers corresponding to the spectral peaks for thick boundary layers.

The spectra for the two configurations 3Dr1N2 (fig. 5) and 3Dr1W2 (fig. 6) with a thicker separating boundary layer display an even larger number of peaks. The analysis is restricted to the peaks identifiable for St<2. The values of the corresponding Strouhal numbers are reported in table 3. For the narrower cavity 3Dr1N2, the twelve first peaks follow the relationship nf_0 with $n = \{1, ..., 12\}$, where $f_0 = f_1$ is the frequency of the first peak. Nevertheless the amplitude repartition is not monotonic, supporting that the peaks are not all harmonics or subharmonics of a single frequency. The dominant frequency, also associated to the acoustic wavelength, is $f_5 = 5f_0$. Noting $f_a = f_2$, and $f_b = f_5$, the serie found previously is f_2, f_3, f_5, f_7, f_8, f_{10}, f_{12}, ... Additional peaks can result from interactions with the low frequency f_0 : $f_1 = f_0$, $f_4 = f_b - f_0$, $f_6 = f_b + f_0$, $f_9 = 2f_b - f_0$, $f_{11} = 2f_b + f_0$, ...

For the wider cavity 3Dr1W2, 17 peaks are detected for St<2. The dominant ones are associated to number 7 and 14 in table 3, corresponding to the fundamenal and its first harmonic. Other significant peaks are observed for St_3, St_4 and St_{11}. The latter frequency is seen to be dominant at the bottom of the cavity (sensor D). The main difference with the case 3Dr1N2 is the presence of two low-frequency components, $f_1 = f_{01}$, and $f_2 = f_{02}$. Noting $f_a = f_3$, and $f_b = f_7$, three patterns of interactions are possible : f_3, f_4, f_7, f_{10}, f_{11}, f_{14}, f_{17} corresponding to f_a, $f_b - f_a$, f_b, $f_b + f_a$, $2f_b - f_a$, $2f_b$, $2f_b + f_a$; the serie f_1, f_5, f_7, f_8, f_{12}, f_{14}, f_{15} corresponding to f_{01}, $f_b - f_{01}$, f_b, $f_b + f_{01}$, $2f_b - f_{01}$, $2f_b$, $2f_b + f_{01}$; and the serie f_2, f_6, f_7, f_9, f_{13}, f_{14}, f_{16} corresponding to f_{02}, $f_b - f_{02}$, f_b, $f_b + f_{02}$, $2f_b - f_{02}$, $2f_b$, $2f_b + f_{02}$. The gray lines on the spectra corroborate this view.

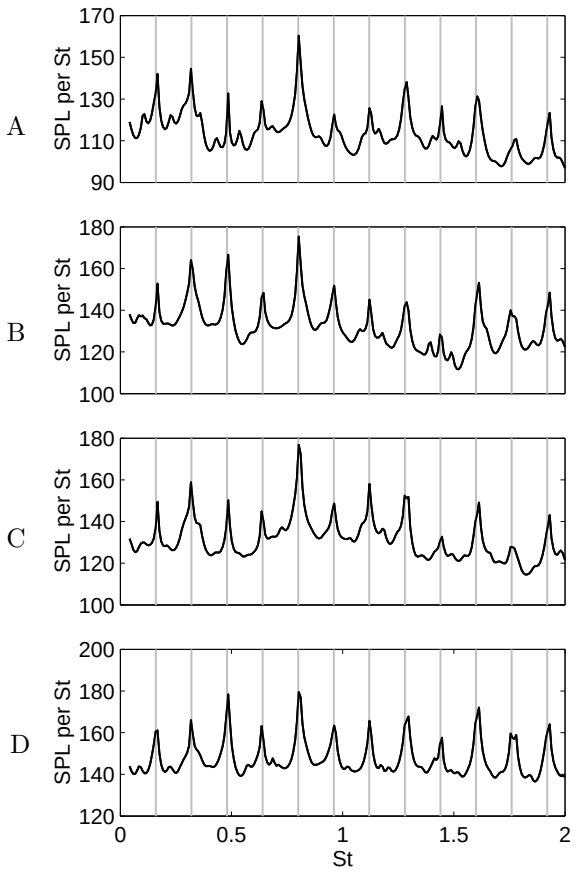

Figure 5: Power spectral density of fluctuating pressure for 3Dr1N2. Same sensors A to D as in fig. 3.

A common feature of the four configurations is the the possible interation between the fundamental frequency f_b and its harmonics, and the low-frequency components, f_a, f_0, or f_{01} and f_{02}. The harmonics are more important when the pressure levels are higher, *i.e.* for the two wider cavities 3Dr1W1 and 3Dr1W2. The value of the Strouhal number associated to f_a is nearly the same for the four configurations, $St_I \sim 0.33$. That of the dominant Strouhal number $f_b L/U_\infty$ is very close for the cases 3Dr1W1, 3Dr1N2, and 3Dr1W2, $St_{II} \sim 0.8$, but is higher for 3Dr1N1, $St_{III} \sim 1.23$, as already noted in

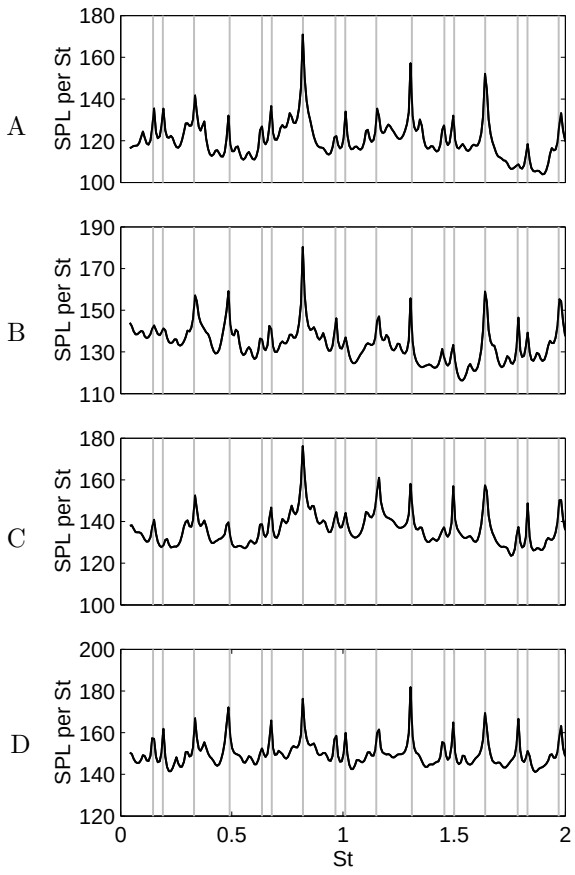

Figure 6: Power spectral density of fluctuating pressure for 3Dr1W2. Same sensors A to D as in fig. 3.

the pictures of the radiated field (fig. 2). The quadratic interactions will be subsequently studied through bispectral analysis in §4.3.

The signal must be stationary to avoid wrong interpretation of the different peaks. Therefore time-frequency analysis is now used to ascertain the effective coexistence of the mutiple tones. It is based on short-time Fourier transforms, defined as :

$$X(t,f) = \int_{-\infty}^{+\infty} x(\tau) w(\tau - t) \mathrm{e}^{-i2\pi f\tau}\, d\tau$$

for a signal $x(t)$, and w denotes the Hann window. The spectrogram is obtained by taking the square of the magnitude of $X(t,f)$. It is calculated by splitting the signal into overlapping segments, windowing each with the Hann function, and calculating a 512 point FFT. A compromise is needed between time and frequency resolution. With a sampling rate of 1.6 MHz and $\Delta f \simeq 850$ Hz, we obtain $\Delta t \simeq 1.5 \times 10^{-4}$ s. The spectrogram of the fluctuating pressure for the 4 configurations and for the sensor B located at the beginning of the shear layer are plotted in figure 7. The frequency content is seen to be stable in time for the three last cases. For the configuration 3Dr1N1, substantial modulations are visible until

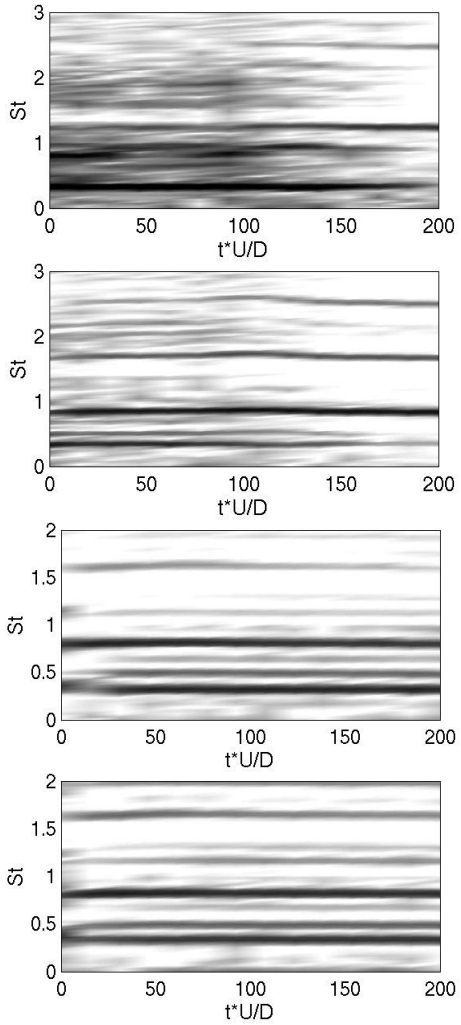

Figure 7: Spectrograms of the fluctuating pressure at the sensor B. From top to bottom, configurations : 3Dr1N1, 3Dr1W1, 3Dr1N2, 3Dr1W2.

the oscillations stabilize at frequency f_b. This suggests a competition between two modes during the transient history. Nevertheless, time-frequency analyses reveal that multiple modes are almost always present in the signals.

3.2 Spectral analysis of the velocity signals

An insight into the flow structure is given by the vorticity snapshots of figure 8. In all cases, the shear layer rolls up after a first oscillation. For the last three cases, one well-formed vortex is visible after the first oscillation, so that a mode II of cavity oscillation is obtained. The first picture for 3Dr1N1 reveals one more vortex, so that it can be associated to a mode III.

The spectra inside the shear layer for each velocity components show the coexistence of the tonal components already found in the pressure spectra. In order to investigate the streamwise evolution of these components, velocity fluctuations have been recorded every

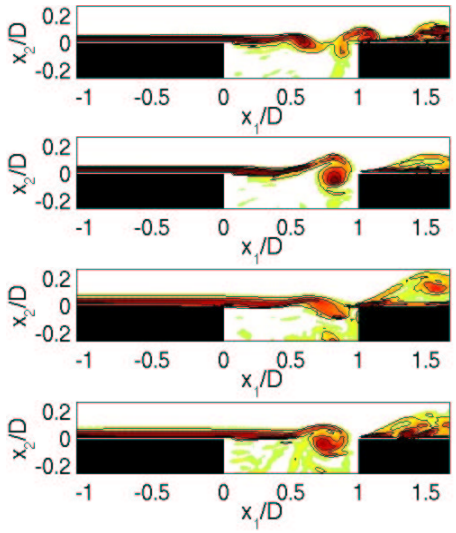

Figure 8: Visualizations of instantaneous vorticity in the midplane $x_3 = 0$ for the four configurations : from top to bottom, 3Dr1N1, 3Dr1W1, 3Dr1N2, 3Dr1W2.

$L/20$ along the lipline $x_2 = 0$ joining the two corners of the cavity. Each spectrum used for deducing the peak amplitudes represents an ensemble average of 7 spectra for 7 spanwise locations, with each of these spectra, in turn, based on about 40 periods of the low frequency f_a. The amplitudes of the i^{th} peak are designated as $(u_{rms})_{M_i}$, $(v_{rms})_{M_i}$, and $(w_{rms})_{M_i}$ for the three velocity components. They are depicted in figures 9 to 12 with the symbols associated in tables 2 and 3.

In all cases, the fundamental frequency, noted previously f_b, clearly dominates. For the streamwise velocity fluctuations, the fundamental component is seen to reach a peak around $x_1/L \simeq 0.5$, decreases, and increases again just before impingement ($x_1/L \simeq 0.9$). For the configurations 3Dr1N2 and 3Dr1W2 with a thicker boundary layer, the lower mode, f_a, can exceed the magnitude associated to f_b, with a maximum value near $x_1/L \simeq 0.75$. For the vertical velocity fluctuations, the predominance of the fundamental is more pronounced. For thinner boundary layer cases, the levels of the first harmonic $2f_b$ are significant, whereas, for the thicker boundary layer cases, the second most important component is f_a. The global levels are close to those found for the streamwise fluctuations, around 8% of U_∞. On the contrary, the levels for the spanwise velocity fluctuations are about one order of magnitude smaller. The amplitudes of all the components of w_{rms} grow in general with increasing x_1/L, indicating a reinforcement of the three-dimensional activity as the downstream corner is approached.

3.3 Streamwise amplification of flow instabilities

Exponential growth region

The growth of the shear layer between the two edges of the cavity is represented in figure 13 by the evolu-

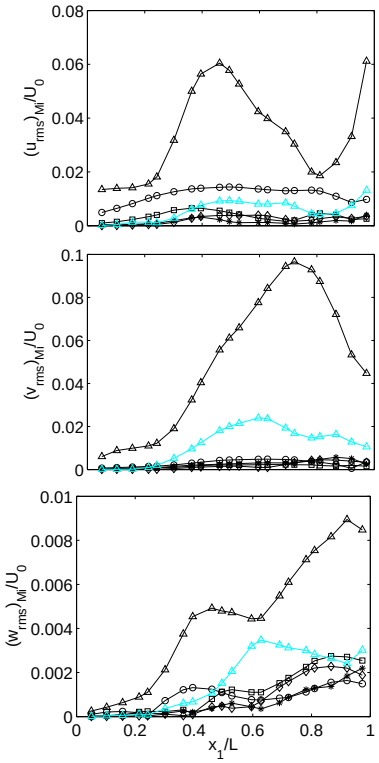

Figure 9: Streamwise evolution of spectral peaks along the lipline for 3Dr1N1. For symbols, see in table 2.

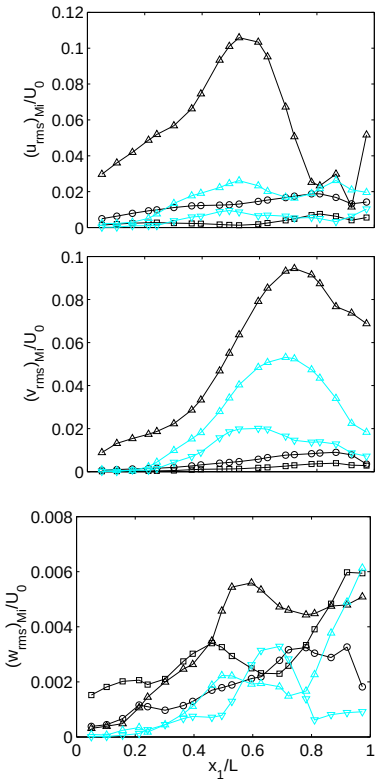

Figure 10: Streamwise evolution of spectral peaks along the lipline for 3Dr1W1. For symbols, see in table 2.

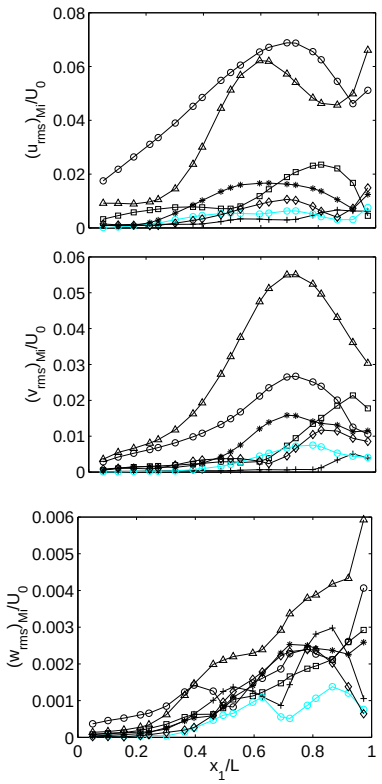

Figure 11: Streamwise evolution of spectral peaks along the lipline for 3Dr1N2. For symbols, see in table 3.

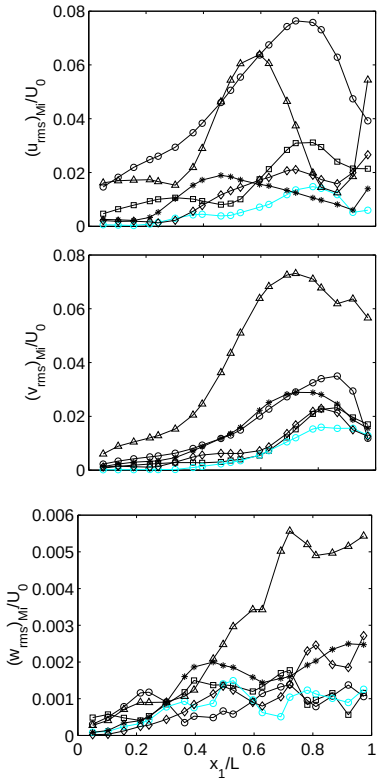

Figure 12: Streamwise evolution of spectral peaks along the lipline for 3Dr1W2. For symbols, see in table 3.

tion of the momentum thickness for the four cases. A short region with a weak growth rate is observed up to $x_1/L \simeq 0.2$ for the configurations with the thinner incoming boundary layer, and up to $x_1/L \simeq 0.35$ for those with the thicker boundary layer. The sudden widening indicates the location of vortex roll-up. After roll-up, the growth is quasi-linear with a similar rate for all cases, $d\delta_\theta/dx_1 \simeq 0.035$, in reasonable agreement with the value found for a turbulent mixing layer. The severe decrease just before the downstream corner is associated to the impingement of flow structures.

Free shear layers are usually characterized by an initial exponential amplification of instabilities, well described by Michalke's linear theory for a parallel flow.[14,15] The shear layer above a cavity displays the features of a forced shear layer but the high levels of acoustic forcing induce a faster roll-up of the Kelvin-Helmholtz vortices, so that the exponential-growth region is shortened. In the simulated configurations, such a region is detected, especially when the separating boundary layer is thicker. To estimate how the impingement feedback influences the early development of the shear layer, the growth rates of the two main components of the vertical velocity fluctuations for the configuration 3Dr1N2 are plotted in semi-log coordinates in figure 14. The estimated growth rate at the fundamental frequency f_{II} agrees well with the predicted growth rate from Michalke's linear spatial theory,[16] or with the experimental values reported by Miksad for a free shear layer,[15] as indicated in table 4. As in the experimental work of Freymuth,[14] or Knisely & Rockwell,[17] the reference momentum thickness, denoted by δ_{θ_m}, is the value at $x_1/L \simeq 0.1$, which is estimated to be near the centre of the exponential-growth region ($\delta_{\theta_m} \simeq 2.6 \times 10^{-5}$ m). The growth rate of the low-frequency component f_{I} is weaker, as predicted by Michalke's theory.

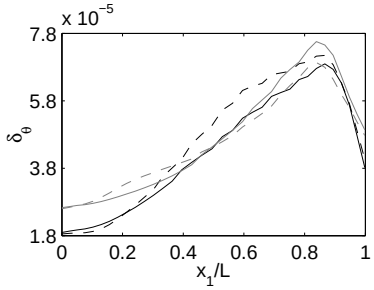

Figure 13: Streamwise evolution of the shear-layer momentum thickness : (——) 3Dr1N1,(– – –) 3Dr1W1, (——) 3Dr1N2, (– – –) 3Dr1W2.

It can be noted, as also emphasized by Knisely & Rockwell, that the initial amplitude of the fluctuations is relatively large ($0.01U_\infty$ for $(v_{rms})_{M_b}$). The acoustic forcing is sufficiently strong to provide non-linear disturbances, whereas the stability theory requires infinitesimal (linear) disturbances. A consequence would be a

smaller simulated growth rate than that predicted by Michalke. For the cases with a thinner incoming boundary layer, the exponential-growth regions exhibit similar characteristics, but are considerably shortened.

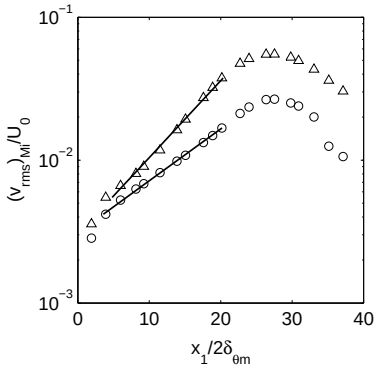

Figure 14: Growth rates of disturbances for mode I (∘) and II (△) in the case 3Dr1N2.

	$\beta = 4\pi \mathrm{St}_{\delta_{\theta m}}$	$-2\alpha_i \delta_{\theta_m}$
mode II	0.13	0.12
Michalke[16]	0.13	0.16
Miksad[15]	0.113	0.11
mode I	0.05	0.08
Michalke[16]	0.05	0.06

Table 4: Spatial growth rates of disturbances for mode I and II in the case 3Dr1N2.

Onset of nonlinearities

The onset of nonlinearity occurs when the disturbance amplitude becomes sufficiently large. The distributions of the peaks of the u_{rms} spectra show an overshoot of the level by as much as $0.1U_\infty$ for a location varying between $x_1/L = 0.4$ and 0.6, so that the nonlinear region extends over the main part of the shear layer. This is accompanied by the appearance of higher harmonics.[15] For instance, in the experiments of Ziada and Rockwell[18] on the mixing layer-edge self-sustained oscillations, $2f_b$, $3f_b$, $4f_b$ components are clearly visible. Even excited shear layers with turbulent initial conditions exhibit higher harmonics with similar features to the initially laminar mixing layer of Miksad. In the present study, the amplitude and the number of harmonics detectable is function of the configuration considered. When the pressure levels are higher, in the wide cases 3Dr1W1 and 3Dr1W2, the harmonics are more marked.

Vortex coalescence

In experiments with a strong forcing,[19,20] subharmonic vortex pairing tends not to occur since the high level of the fundamental delays the growth of the subharmonic. Nevertheless, in certain cases, subharmonic pairing have be observed.[21] It seems to occur in the configuration 3Dr1W1, as shown by the figure 6 of ref.[12] This fusion is less identifiable than vortex pairings in free mixing layer, but can be associated to the early stages of a subharmonic pairing. However, note that the low-frequency components are not always related to the vortex coalescence, and must originate from an other mechanism.

Another coalescence possibility is the simultaneous fusion of a number of vortices, referred to as collective interaction by Ho and Nosseir,[22] which can participate in the selection of the dominant frequency.[23] The necessary condition for this interaction is a high-amplitude low-frequency excitation. This is not the case in the present configurations because the Strouhal number based on the momentum thickness is $\mathrm{St}_\theta = 0.012$, near the value 0.017 for the most unstable frequency of hyperbolic-tangent velocity profile. The initial vortex-formation frequency is seen to match the forcing frequency.

4. The origins of the multiple frequency content

4.1 Intermittency and mode-switching

Intermittency of the shear-layer turbulence may lead to multiple modes which apparently coexist. The self-sustained oscillations may then exist in more than one metastable state, jumping between the different modes. This conjecture[20] has however few clear experimental illustrations. An alternance between modes, called *mode-switching* is for instance observed in the experiments of Cattafesta *et al.*[24] These authors provide pictures of the shear layer, showing that the size of the dominant structures can change with time, and that switching between modes I, II and III can occur. Note that a kind of mode-switching has been identified in a previous 3-D simulation[23] of a turbulent cavity flow at a Reynolds number $\mathrm{Re}_L = 1.5 \times 10^5$, higher than in the present simulations. The time-averaged spectra showed the existence of two peaks, but the analysis reveals that the alternance of modes followed a well-defined cycle with a succession of the two modes, so that they cannot be separated by a time-frequency method.

In the present investigation, the time-frequency analyses of figure 7 do not show any significant change in the frequency content. This supports that the phenomenon of switching is not observed in the present cavity flows at Reynolds numbers $\mathrm{Re}_L = 2.9 \times 10^4$. It is conjectured that it is more likely to be found in fully turbulent shear layers, *i.e.* at higher Reynolds numbers. The vortices are then clusters of small scales rather than single rolls. The jump from one mode to the other can proceed from a reorganisation of the clusters.

4.2 Cycling patterns in the impingement process

The patterns of interaction at impingement must be compatible with the unsteady signals, modulated by the low-frequency components. This is checked for the con-

figuration 3Dr1N2, where numerous peaks are observed in the spectra of figure 5. The temporal evolution of the vertical velocity at the beginning of the shear layer is presented in figure 15, and exhibits a five-cycle repetition. The regularity of this five-cycle pattern is an indication of a relatively stable phasing between the components. Such a regular pattern is rare in experimental signals. For low Reynolds number experiments in water, Knisely & Rockwell[17] however observed a good reproductibility of the cycling pattern, even if a kind of intermittency was noted. It is thought, as already addressed in §4.1, that the wide range of turbulent scales at high Reynolds number may have an influence on the level of intermittency. When the phasing between the different periodic components is perturbed, it can result in a burst of random oscillations, as observed by Neary & Stephanoff.[25]The cycling can reorganize later.

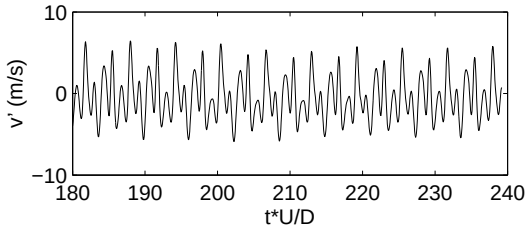

Figure 15: Instantaneous traces of the vertical velocity fluctuations at the sensor B for 3Dr1N2.

A sequence of the five-cycle repetition is visualized. The norm of the vorticity is depicted in figure 16 during five successive cycles with two pictures per cycle. The traces of the fluctuating pressure near the downstream corner and of the vertical velocity fluctuations just after the separation point are represented below the pictures. The letters (a) to (j) on the traces indicate the instants corresponding to each of the vorticity views.

In the left column, the center of vortices is located near the downstream corner, so that a maximum negative peak is found in the pressure trace. In the right column, the vortices have later impacted upon the downstream corner. A careful study of the five successive cycles reveals that the impinging vortex is located at a lower vertical position on the edge in figures 16(c), (e), (i) than in (a) or (g). Consequently, a larger portion of the vortices is severed by the edge in figure 16(d), (f), (j) than in (b) and (h). The apparent escapes of the impinging vortices in the first and fourth cycles correspond to a stronger negative peak in the pressure trace at the sensor C, located just above the downstream edge. The vortex pattern described here and consequently the form of the velocity trace tend to be repetitive.

4.3 Nonlinear interactions between cavity modes

Since the power spectrum does not provide information on the phase, higher-order spectra (HOS) are required to shed light on nonlinearities in the signal generation. Kim *et al.*[26,27] have shown that implementation

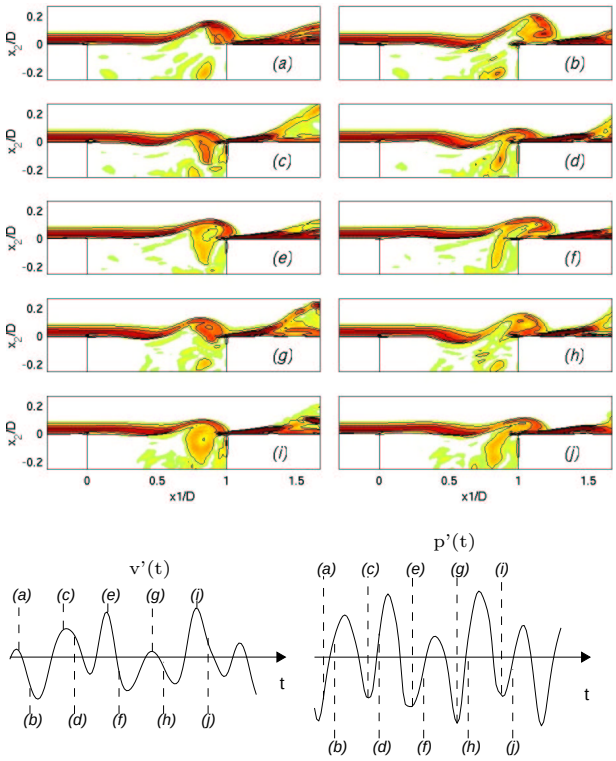

Figure 16: Ten snapshots of the vorticity in the mid-plane $x_3 = 0$ during five successive cycles for 3Dr1N2. Below, temporal traces of the fluctuating velocity at the sensor B (on the left) and pressure at the sensor C (on the right) for the five cycles visualized.

of the third-order spectrum, known as the bispectrum, provides a method for distinguishing between self-excited and nonlinearly coupled modes. This method has been applied for self-sustained cavity oscillations by Isaacson & Marshall[28] in the case of a cavity for an internal turbulent flow, by Knisely & Rockwell[17] for a low Reynolds number cavity flow in water, and by Cattafesta *et al.*[24] for high Reynolds number cavity air flows. The bispectrum can be evaluated as the two-dimensional Fourier transform of the third-order cumulant :

$$C(\tau_i, \tau_j) = \mathrm{E}[x(t)x(t+\tau_i)x(t+\tau_j)]\,,$$

or as :

$$B(f_i, f_j) = \lim_{T\to\infty} \frac{1}{T}\mathrm{E}[X(f_i)X(f_j)X^*(f_i+f_j)]\,,$$

where $X(f)$ is the Fourier transform of the signal $x(t)$, T is the time duration of the signal, the asterisk denotes a complex conjugate, and E represents the expectation value. When nonlinear coupling and phase coherence exists between two frequencies f_i and f_j, an interaction peak appears in the bispectrum plot. Only a triangular domain is usually represented owing to the symmetry of the Fourier components. As in spectral analysis, a compromise is required between frequency resolution and the

number of averages. In the present study, 2000 samples are used, segmented in three parts overlapped by 50%, and an average over 11 spanwise sensors is performed. It is sufficient to resolve fine interaction peaks, but not to achieve convergence of the bicoherence spectrum. The bicoherence, lying between zero and unity, would have been helpful to compare the relative levels of the numerous possible interactions.

In all the cases investigated, the bispectra, depicted for St< 2 in figure 17, exhibit several significant peaks indicating the presence of coupled frequencies. The gray lines indicate the peak Strouhal numbers, listed in tables 2 and 3. For 3Dr1N1, a peak at (f_a, $f_b - f_a$) indicates that f_a and $f_b - f_a$ interact to give f_b. The peak located at (f_b, f_b) correspond to the interaction of the fundamental with itself to generate the harmonic $2f_b$. The other peaks at (0,f_a) and (0,f_a) could result from non exactly centered signals. For the case 3Dr1W1, several peaks are shown. The strong peak at (f_b, f_b) generates the first harmonic. Numerous sum or difference interactions between the mode I, f_a, and the mode II, f_b are observed :

$f_a + (f_b - f_a) \rightarrow f_b$ $\quad$ $(f_b - f_a) + 2f_b \rightarrow (3f_b - f_a)$

$f_a + f_b \rightarrow (f_b + f_a)$ $\quad$ $2f_b - (f_b - f_a) \rightarrow (f_b + f_a)$

$f_b - f_a \rightarrow (f_b - f_a)$ $\quad$ $f_b + (f_b + f_a) \rightarrow (2f_b + f_a)$

$(f_b + f_a) - f_a \rightarrow f_b$ $\quad$ $(f_b + f_a) - f_b \rightarrow f_a$

$f_a + (2f_b - f_a) \rightarrow 2f_b$ $\quad$ $f_b + (2f_b - f_a) \rightarrow (3f_b - f_a)$

$(f_b - f_a) + f_b \rightarrow (2f_b - f_a)$ $\quad$ $(2f_b - f_a) - f_b \rightarrow (f_b - f_a)$

$f_b - (f_b - f_a) \rightarrow f_a$ $\quad$ $f_b + 2f_b \rightarrow 3f_b$

$(f_b - f_a) + (f_b + f_a) \rightarrow 2f_b$ $\quad$ $2f_b - f_b \rightarrow f_b$, ...

For the two last cases 3Dr1N2 and 3Dr1W2, numerous peaks are also detected, indicating that the different components reinforce through nonlinear interaction. The strong peak noted at (f_a, f_b) and (f_a, $f_b - f_a$) are consistent with the series proposed in §3.1. In these cases, f_a being the mode I and f_b the mode II of the Rossiter feedback loop, the coexistence of several Rossiter modes may be sustained by quadratic interactions.

5. Conclusion

The coexistence of multiple tones in cavity flow spectra is investigated in four laminar non-resonant configurations by Direct Noise Computation. Time-frequency analysis shows that these tones are present simultaneously, and do not result from mode-switching. The different modes are rather coupled, as indicated by the bispectra of the fluctuating pressure. A detailed study reveals remarkably ordered patterns of interacting vorticity in the vicinity of the downstream corner, involving an alternance of severe clippings and partial escapes. The effects of these organized vortex-corner interactions on the initial separating shear layer will sustain the cycling pattern, thus the multiple frequency content. In future

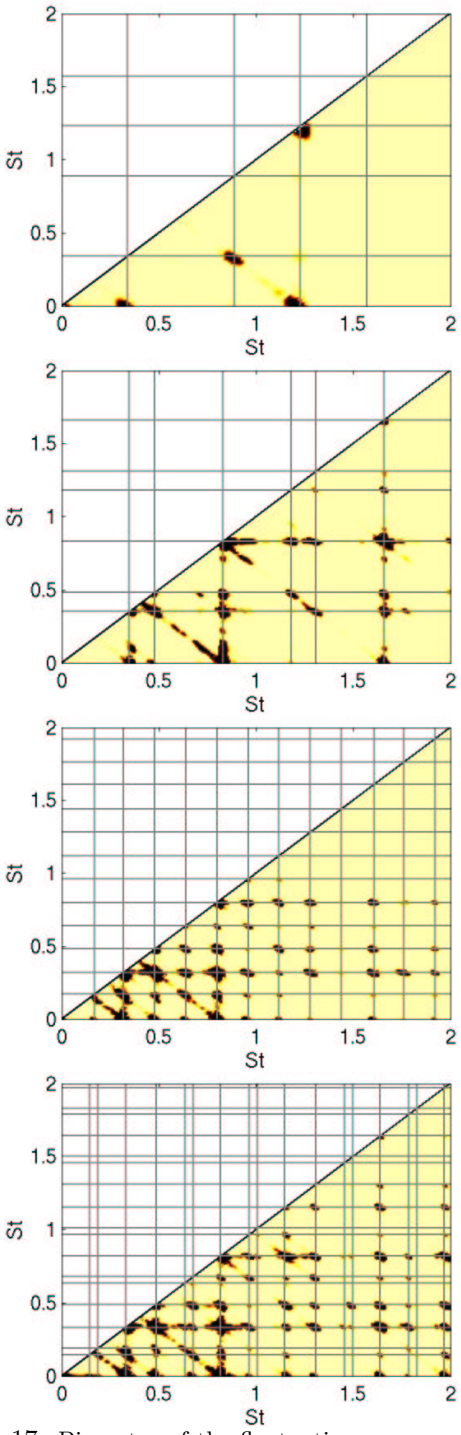

Figure 17: Bispectra of the fluctuating pressure at the sensor B. From top to bottom, configurations : 3Dr1N1, 3Dr1W1, 3Dr1N2, 3Dr1W2.

works, the study of the overall phase relationships between the two corners of the cavity may help to further understand the feedback phenomenon.

Another important issue is the influence of the studied parameters. First, changing the width W of the cavity modifies the cavity oscillations. The higher sound levels observed for wider cavities can be associated to a higher spanwise coherence, reinforcing the feedback strength. Second, the thickness of the incoming boundary layer is seen to drive the growth of instabilities in the separating shear layer, and thus the size of the vortices. For the narrow cavities, a mode III is thus excited for the higher ratio L/δ_θ whereas a mode II is sustained for the lower ratio. The pertinent parameter for the mode selection is therefore L/δ_θ. Another remark concerns the influence of the Reynolds number. In these low-Reynolds number configurations, no mode-switching is detected, and a regular repetition of cycling patterns is noted. For turbulent conditions, the wider range of scales may induce intermittency in the signals, and the clusters of small scales are more likely to lead to mode-switching.

Acknowledgments

Supercomputer time is supplied by Institut du Développement et des Ressources en Informatique Scientifique (IDRIS - CNRS).

References

[1] Plumblee, H.E., Gibson, J.S. & Lassiter, L.W. A theoretical and experimental investigation of the acoustic response of cavities in an aerodynamic flow. *Rep.* WADD-TR-61-75, U.S. Air Force, 1962.

[2] Elder, S.A., Farabee, T.M. & DeMetz, F.C., 1982, Mechanisms of flow-excited cavity tones at low mach number, *J. Acoust. Soc. Am.*, **72**(2), p. 532–549.

[3] Rossiter, J.E. Wind-tunnel experiments on the flow over rectangular cavities at subsonic and transonic speeds. Technical Report 3438, *Aeronautical Research Council Reports and Memoranda*, 1964.

[4] Powell, A., 1961, On the edgetone, *J. Acoust. Soc. Am.*, **33**(4), p. 395–409.

[5] Blake, W.K. *Mechanics of flow-induced sound and vibration*, volume 1: General concepts and elementary sources, chapter 3, p. 130–149. Academic Press, Inc, 1986.

[6] Meissner, M., 1993, Experimental investigation of discrete sound production in deep cavity exposed to airflow, *Archives of Acoustics*, **18**(1), p. 131–156.

[7] Tam, C.K.W. & Block, P.J.W., 1978, On the tones and pressure oscillations induced by flow over rectangular cavities, *J. Fluid Mech.*, **89**(2), p. 373–399.

[8] Ahuja, K.K. & Mendoza, J., 1995, Effects of cavity dimensions, boundary layer, and temperature in cavity noise with emphasis on benchmark data to validate computational aeroacoustic codes, NASA CR-4653.

[9] Gharib, M. & Roshko, A., 1987, The effect of flow oscillations on cavity drag, *J. Fluid Mech.*, **177**, p. 501–530.

[10] Bogey, C. & Bailly, C., 2002, A family of low dispersive and low dissipative explicit schemes for computing aerodynamic, *AIAA Paper 2002-2509*.

[11] Bogey, C. & Bailly, C., 2002, Three-dimensional non-reflective boundary conditions for acoustic simulations : far field formulation and validation test cases, *Acta Acustica*, **88**, p. 463–471.

[12] Gloerfelt, X., Bogey, C., Bailly, C. & Juvé, D., 2002, Aerodynamic noise induced by laminar and turbulent boundary layers over rectangular cavities, *AIAA Paper 2002-2476*.

[13] Marple, S.L. Jr, 1987, *Digital spectral analysis with applications*, Prentice-Hall, Englewood Cliffs, N.J.

[14] Freymuth, P., 1966, On transition in a separated laminar boundary layer, *J. Fluid Mech.*, **25**(4), p. 683–704.

[15] Miksad, R.W., 1972, Experiments on the nonlinear stages of free-shear-layer transition, *J. Fluid Mech.*, **56**(4), p. 695–719.

[16] Michalke, A., 1965, On spatially growing disturbances in an inviscid shear layer, *J. Fluid Mech.*, **23**(3), p. 521–544.

[17] Knisely, C. & Rockwell, D., 1982, Self-sustained low frequency components in an impinging shear layer, *J. Fluid Mech.*, **116**, p. 157–186.

[18] Ziada, S. & Rockwell, D., 1981, Generation of higher harmonics in a self-oscillating mixing layer-wedge system, *AIAA Journal*, **20**, p. 196–199.

[19] Sarohia, V., 1977, Experimental oscillations in flows over shallow cavities, *AIAA Journal*, **15**(7), p. 984–991.

[20] Rockwell, D., 1983, Oscillations of impinging shear layers, *AIAA Journal*, **21**(5), p. 645–664.

[21] Hussain, A.K.M.F. & Zaman, K.B.M.Q., 1978, The free shear layer tone phenomenon and probe interference, *J. Fluid Mech.*, **87**(2), p. 349–383.

[22] Ho, C.-M. & Nosseir, N.S., 1981, Dynamics of an impinging jet. Part 1. The feedback phenomenon, *J. Fluid Mech.*, **105**, p. 119–142.

[23] Gloerfelt, X., Bogey, C. & Bailly, C., 2003, Numerical evidence of mode switching in the flow-induced oscillations by a cavity. Submitted to *Int. J. of Aeroacoustics*. See also CEAS workshop from CFD to CAA, nov. 2002, Athens, Greece.

[24] Cattasfesta III, L.N., Garg, S., Kegerise, M.A. & Jones, G.S., 1998, Experiments on compressible flow-induced cavity oscillations, *AIAA Paper 98-2912*.

[25] Neary, M.D. & Stephanoff, K.D., 1987, Shear-layer-driven transition in a rectangular cavity, *Phys. Fluids*, **30**(10), p. 2936–2946.

[26] Kim, Y.C. & Powers, E.J., 1978, Digital bispectral analysis of self-excited fluctuation spectra, *Phys. Fluids*, **21**(8), p. 1452–1453.

[27] Kim, Y.C., Beall, J.M., Powers, E.J. & Miksad, R.W., 1980, Bispectrum and nonlinear wave coupling, *Phys. Fluids*, **23**(2), p. 258–263.

[28] Isaacson, L.K. & Marshall, A.G., 1983, Nonlinear resonant interactions in internal cavity flow, *AIAA Journal*, **21**(5), p. 785–786.